Rational Design Principles of the Quantum Anomalous Hall Effect in Superlatticelike Magnetic Topological Insulators

Hongyi Sun,[1] Bowen Xia,[1] Zhongjia Chen,[1,2] Yingjie Zhang,[1] Pengfei Liu,[1] Qiushi Yao,[1] Hong Tang,[1] Yujun Zhao,[2] Hu Xu,[1] and Qihang Liu[1,3,4,*]

[1]*Shenzhen Institute for Quantum Science and Technology and Department of Physics, Southern University of Science and Technology (SUSTech), Shenzhen 518055, China*
[2]*Department of Physics, South China University of Technology, Guangzhou 510640, China*
[3]*Guangdong Provincial Key Laboratory for Computational Science and Material Design, Southern University of Science and Technology, Shenzhen 518055, China*
[4]*Center for Quantum Computing, Peng Cheng Laboratory, Shenzhen 518055, China*

(Received 29 May 2019; published 28 August 2019)

As a paradigmatic phenomenon in condensed matter physics, the quantum anomalous Hall effect (QAHE) in stoichiometric Chern insulators has drawn great interest for years. Using model Hamiltonian analysis and first-principles calculations, we establish a topological phase diagram and map different 2D configurations to it, which are taken from the recently grown magnetic topological insulators $MnBi_4Te_7$ and $MnBi_6Te_{10}$ with superlatticelike stacking patterns. These configurations manifest various topological phases, including the quantum spin Hall effect with and without time-reversal symmetry and QAHE. We then provide design principles to trigger the QAHE by tuning experimentally accessible knobs, such as the slab thickness and magnetization. Our work reveals that superlatticelike magnetic topological insulators with tunable exchange interactions are an ideal platform to realize the long-sought QAHE in pristine compounds, paving a new path within the area of topological materials.

DOI: 10.1103/PhysRevLett.123.096401

The combination of magnetism and electronic structure topology in condensed matter systems provides fruitful ground for exploring exotic quantum phenomena [1–3]. Among these phenomena, the quantum anomalous Hall effect (QAHE), induced by spontaneous magnetization without an extrinsic magnetic field, has been sought for years because its dissipationless edge state holds the potential to realize next-generation electronic devices with ultralow power cost [4,5]. The QAHE was first observed in Cr-doped topological insulator (TI) thin films, but only at a low temperature of approximately 100 mK [6]. Therefore, much effort, especially theoretical proposals [7–15], has been put into 2D stoichiometric magnetic insulators with a nontrivial Chern number (i.e., Chern insulators) to realize the QAHE at a higher temperature, yet without solid experimental confirmation.

Recent breakthroughs in this direction have been made due to the growth technology of 2D ferromagnetic (FM) semiconductors [16,17] and, more importantly, the intrinsic 3D magnetic TI $MnBi_2Te_4$, a magnetic analogue to the time-reversal symmetry (T) preserved TI Bi_2Te_3 comprising stacked van der Waals (VdW) connected sublayers. $MnBi_2Te_4$ in its antiferromagnetic (AFM) ground state (A-type AFM with the moments aligned in the z direction) was predicted and shortly experimentally verified to be a Z_2 AFM TI protected by a combined T and fractional translation operation symmetry [18–21]. Later, quantized Hall conductance was observed for $MnBi_2Te_4$ films down to 5-6 septuple layers [22,23]. Although 2D $MnBi_2Te_4$ multilayers with uncompensated AFM configurations are also predicted to be Chern insulators [24], a magnetic field of 5˜10 T is required to align the spins to an FM state [22,23]. Strictly speaking, the QAHE occurs without a magnetic field because it originates from the topologically protected chiral edge states of a Chern insulator [5]. The external magnetic field produces two types of ambiguity: the contribution from the quantized Landau levels, i.e., the quantum Hall effect [25], and the possible topological transition from a normal insulator (NI) to a Chern insulator induced by the Zeeman exchange field [26]. Hence, to obtain an ideal QAHE system with, if necessary, a sufficiently small magnetic field, a better understanding of the route to achieve the QAHE with experimentally tunable "knobs" and realistic material candidates is highly desirable.

In this Letter, we investigate the topological phase transitions of 2D magnetic systems and how to rationally design quantum anomalous Hall insulators. Starting from an effective model of a 3D T-preserved TI (such as Bi_2Te_3) under an exchange field, we present solutions for 2D thin films and a phase diagram containing various topological states, including the T-preserved quantum spin Hall effect (QSHE) [27,28], T-broken QSHE [29], and QAHE phases. For material realization, we are inspired by the recent growth of $MnBi_4Te_7$ and $MnBi_6Te_{10}$ single crystals [30,31], which are in essence 1:1 and 1:2 superlattices composed of a $MnBi_2Te_4$ septuple layer (denoted "A") and a Bi_2Te_3 quintuple layer (denoted "B"), respectively. Owing to the diversity of the 2D configurations of $MnBi_4Te_7$ and $MnBi_6Te_{10}$ compared with $MnBi_2Te_4$, according to first-principles calculations, the combinations of A and B building blocks can realize all the topological phases in our phase diagram. For example, ABA in its FM state exhibits the QAHE, while AB and BAB exhibit the T-broken QSHE. Since the Bi_2Te_3 buffer layer effectively decreases the AFM coupling between two neighboring A layers, the magnetic field required to trigger the QAHE is orders of magnitude weaker than that for $MnBi_2Te_4$ thin films. Furthermore, we illustrate the possibilities to manipulate the topological phase transitions in the phase diagram either horizontally or vertically through band gap engineering.

Topological phase diagram from the 2D effective model.—Starting from the 4×4 model Hamiltonian of the T-preserved 3D TIs Bi_2Se_3 and Bi_2Te_3 [32], we scale it down to the 2D limit by replacing k_z with the ∂_z operator and then add a uniform exchange field. The resultant model Hamiltonian is

$$H_{2D} = \epsilon(\boldsymbol{k}) + \begin{pmatrix} M(\boldsymbol{k}) + gM & B_0\partial_z & 0 & A_0k_- \\ B_0\partial_z & -M(\boldsymbol{k}) + gM & A_0k_- & 0 \\ 0 & A_0k_+ & M(\boldsymbol{k}) - gM & -B_0\partial_z \\ A_0k_+ & 0 & -B_0\partial_z & -M(\boldsymbol{k}) - gM \end{pmatrix}, \tag{1}$$

where $\epsilon(\boldsymbol{k}) = C_0 - C_1\partial_z^2 + C_2(k_x^2 + k_y^2)$ and $M(\boldsymbol{k}) = M_0 - M_1\partial_z^2 + M_2(k_x^2 + k_y^2)$. The Zeeman effect is characterized by exchange field M along the z axis and the effective g factor. This Hamiltonian, Eq. (1), is invariant under inversion symmetry. The structural inversion asymmetry (SIA) effect is not included here but will be discussed later.

Following the approach introduced by Ref. [33], we then numerically solve the continuous model Hamiltonian Eq. (1) by taking open boundary conditions with the film thickness L in the z direction. Consequently, the topological phase diagram as functions of L and the magnetization gM is obtained, as shown in Fig. 1(a) [34]. The boundary separating different phases is the trajectory of the zero gap at the Γ point, indicating that the topological phase transition must be accompanied by gap closing and reopening. We next determine the topological properties of each area. Taking a fixed L and only four bands around the Fermi level, Eq. (1) is reduced to a block-diagonal Hamiltonian with two decoupled spin channels, in an equivalent form to that discussed in Refs. [26,35]:

$$\begin{aligned} H_{\text{eff}}(\boldsymbol{k}) = {} & (E_0 - Dk^2)\tau_0\sigma_0 + (\Delta - Bk^2)\tau_z\sigma_z \\ & - \gamma\tau_0(k_x\sigma_y - k_y\sigma_x) + gM\tau_0\sigma_z, \end{aligned} \tag{2}$$

where $\boldsymbol{\sigma}$ denotes the Pauli matrices for spin and $\boldsymbol{\tau}$ for the bonding and antibonding states of the two surfaces. The other parameters of Eq. (2) as functions of L are numerically solved using Eq. (1), as shown in the Supplemental Material, Sec. I [36]. Thus, the Chern numbers of the two spin channels can be analytically solved as $C_+ = \frac{1}{2}[\text{sgn}(\Delta + gM) + \text{sgn}(B)]$ and $C_- = \frac{1}{2}[\text{sgn}(-\Delta + gM) - \text{sgn}(B)]$. The Chern number of the entire system is $C = C_+ + C_- = \frac{1}{2}[\text{sgn}(\Delta + gM) + \text{sgn}(-\Delta + gM)]$, while the spin Chern number (for τ_z) is $C_s = C_+ - C_- = \frac{1}{2}[\text{sgn}(\Delta + gM) - \text{sgn}(-\Delta + gM)] + \text{sgn}(B)$.

The phase diagram is then established according to the topological invariants.

T is only preserved when $M = 0$, for which the topological nature of the thin film exhibits an oscillatory behavior between the NI and T-preserved QSHE phases [49,50]. With a finite magnetization $|gM| < \Delta$, no gap

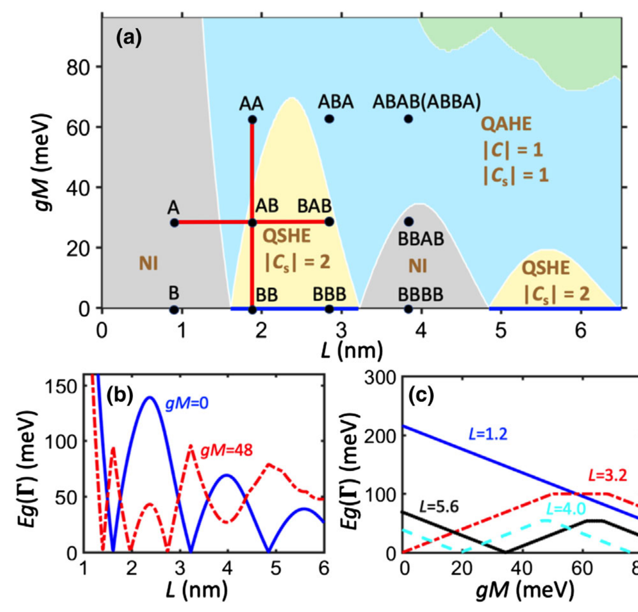

FIG. 1. (a) Topological phase diagram in the 2D limit of a 3D TI under an exchange field in terms of the film thickness L and magnetization gM. Various phases, including the NI (gray area), T-preserved QSHE (blue line), T-broken QSHE (yellow area), and QAHE (cyan area), are shown. The DFT-calculated 2D configurations composed of $MnBi_2Te_4$ (A) and Bi_2Te_3 (B) building blocks are also mapped on the phase diagram (see also Table I and Fig. 2). (b),(c) Energy gap at the Γ point $E_g(\Gamma)$ as functions of (b) L and (c) gM.

closing occurs between the T-preserved QSH and T-broken QSH phases, indicating that they are equivalent topological phases characterized by the same spin Chern numbers. Several observations can be drawn from Fig. 1. First, a sufficiently large M can drive either the NI or QSH insulator to the QAHE territory, consistent with Ref. [26]. Therefore, even if the Landau level effect can be excluded, the magnetic-field-induced quantized Hall conductance is ambiguous in that the magnetic field can trigger the QAHE by such a phase transition. Second, the phase transition between the NI and T-broken QSHE phases is inevitably accompanied by a QAHE region, which can be understood by the evolution of band inversion for different spin channels. From the NI to T-broken QSHE phases, in which the two spin channels are nonequivalent, the subsequent band inversion by tuning of the order parameter L naturally leads to a QAHE region with inverted band order for only one spin channel. Third, the critical points along the L axis are triple-phase points among the NI, QSHE, and QAHE phases. These points are the only connection between the NI and QSHE phases, while a tiny magnetization drives the phase to the QAHE region [26,35]. Finally, for a thick slab and strong magnetization, another trajectory for $E_g(\Gamma) = 0$ exists, depicting an island with a distinguished topological phase, because the subbands of the quantum well system with higher energy move to the Fermi level due to the exchange field, thus inducing another band inversion. This area is not our focus here because experimentally realizing it is challenging.

The band gaps at the Γ point $E_g(\Gamma)$ as functions of L and gM are shown in Figs. 1(b) and 1(c), respectively. For $M = 0$, $E_g(\Gamma)$ oscillates with L, with a gradually decreasing amplitude approaching zero [51,52]. The oscillation period is $\sim\pi\sqrt{M_1/|M_0|}$ (1.6 nm). With nonzero magnetization, $E_g(\Gamma)$ remains open above a certain thickness, and the number of zero-gap nodes is determined by the number of NI or QSHE regions passed by in the phase diagram. For example, the evolution of $E_g(\Gamma)$ at $gM = 48$ meV indicates an NI-QAHE-QSHE-QAHE phase transition. In contrast, with a fixed L, $E_g(\Gamma)$ generally closes only once by increasing M within a moderate range, corresponding to the transition between the NI (or QSHE) and QAHE phases.

Realizing various topological phases with $MnBi_2Te_4$ (*A*) *and* Bi_2Te_3 (*B*) *building blocks.*—Our material realization of different topological phases is inspired by the recent growth of $MnBi_4Te_7$ and $MnBi_6Te_{10}$ single crystals [30,31], formed as superlattices with AB and ABB stacking patterns, where A and B are building blocks of the 3D AFM TI $MnBi_2Te_4$ and 3D nonmagnetic TI Bi_2Te_3, respectively. Density functional theory (DFT) calculations are performed with the presence of spin-orbit coupling (SOC); the details are provided in Supplemental Material, Sec. II [36]. As shown in Fig. 2(a) and Table I, we only consider the 2D configurations that correspond to certain fragments of the 3D parent $MnBi_4Te_7$ or $MnBi_6Te_{10}$ for ease of exfoliation. The exfoliation energy of these slabs is approximately

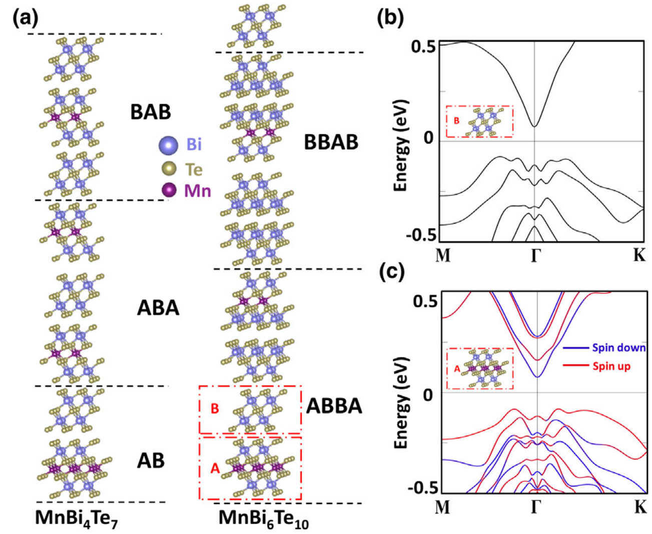

FIG. 2. (a) Crystal structures of $MnBi_4Te_7$ and $MnBi_6Te_{10}$ with their different fragments (marked by black dashed lines) that can be exfoliated as 2D structures. The red dashed boxes denote the A ($MnBi_2Te_4$ septuple layer) and B (Bi_2Te_3 quintuple layer) building blocks. (b) Band structure of the B layer. (c) Band structure of the A layer with the projection of spin operator σ_z. Red and blue denote spin-up and spin-down channels, respectively.

22 meV/Å^2 (see Supplemental Material, Sec. III) [36], comparable to that of graphite (18 meV/Å^2). For the configurations with only one A layer, the FM phase is the ground state, while for those with two A layers, the FM phase can be stabilized by a tiny magnetic field because its total energy is only ~0.1 meV (or less) higher than the ground state (see Table I), i.e., through AFM coupling between neighboring A layers. Because of the role of the B layer as a spacer, the out-of-plane saturation field of bulk $MnBi_4Te_7$ was measured to be 0.22 T, 40 times lower than that of $MnBi_2Te_4$ [30]. Noting that the AFM phases with an even number of A layers are candidates for axion insulators with the zero-plateau QAHE [18,24], we next focus on FM phases for all configurations. The diversity of the film thicknesses and magnetization strengths helps us establish a parametrized connection between different topological phases based on the phase diagram and thus the QAHE design principle.

To map the configurations into the phase diagram, we first demonstrate that an A monolayer can be effectively described as a B monolayer plus an exchange field. Structurally, an A layer is formed by a B layer with MnTe intercalation. For a nonmagnetic B layer, the coexistence of inversion symmetry and T ensures spin degeneracy for the full Brillouin zone [Fig. 2(b)], while for an A layer, the magnetization of Mn lifts the spin degeneracy [Fig. 2(c)]. The Mn-3d^5 states are located far from the Fermi level (see Supplemental Material, Sec. IV [36]), implying that the main effect of Mn is to introduce a Zeeman exchange field to Bi_2Te_3. To prove this, we project

TABLE I. Properties of considered 2D configurations, including the number of layers, stacking pattern of building blocks, parent 3D compounds, energy difference between FM and A-type AFM phases (if the configuration has more than one A layer) $\Delta E = E_{\mathrm{FM}}\text{-}E_{\mathrm{AFM}}$, energy gap at the Γ point $E_g(\Gamma)$, Chern number (C), and spin Chern number (C_s). N/A means that there is no A-type AFM phase and the FM phase is the ground state.

No. of layers	Stacking	Parent compound	ΔE (meV/Mn)	$E_g(\Gamma)$ (meV)	C	C_s
2	*AB*	Both	N/A	158.9	0	2
3	*ABA*	$MnBi_4Te_7$	0.17	37.4	1	1
	BAB	$MnBi_4Te_7$	N/A	122.9	0	2
	ABB	$MnBi_6Te_{10}$	N/A	36.7	0	2
4	*ABAB*	$MnBi_4Te_7$	0.15	12.8	1	1
	ABBA	$MnBi_6Te_{10}$	0.03	77.1	1	1
	BBAB	$MnBi_6Te_{10}$	N/A	16.0	0	0

the band eigenstates onto σ_z, i.e., $\langle\varphi_n(\boldsymbol{k})|\sigma_z|\varphi_n(\boldsymbol{k})\rangle$, to distinguish the spin-up and spin-down channels. For the four bands around the Fermi level in the vicinity of Γ, the spin-up channels shift upwards in energy compared with the spin-down channels, and the spin splittings for the valence and conduction bands (0.15 and 0.16 eV, respectively) are almost the same. Hence, we conclude that for the four-band low-energy Hamiltonian, an A layer can be well described by a B layer under an exchange field, with a similar g factor for different orbitals.

The topological properties of the 2D configurations, characterized by their Chern numbers (C) and spin Chern numbers (C_s), are listed in Table I. Figure 3 presents three representative topological phases, including the *BB* T-preserved QSHE (bilayer Bi_2Te_3), *AB* T-broken QSHE, and *ABA* QAHE phases. All three configurations have explicit band inversions between Bi-p and Te-p orbitals but distinct features for the edge states. Specifically, for *BB*, a clear gapless Dirac cone protected by T exists, leading to a quantized spin Hall conductance in the bulk gap. In comparison, for *AB*, the T breaking slightly gaps the Dirac cone, consistent with the previous prediction [29]. Thus, the edge states consist of two counterpropagating channels with each almost spin polarized, resulting in a spin Hall conductance plateau similar to that in the clean limit but that may not be robust to disorder. Although the Z_2 index does not apply to systems without T, what makes *AB* topologically nontrivial is its nonzero spin Chern number, which remains valid when T is broken and corresponds to a gapless projected spin spectrum [53]. For the *ABA* configuration, the green squares in Fig. 3(h) show that two branches emerge from the valence band at $k_a = 0$ but only one occurs at $k_a = 2\pi$, indicating that the other branch connects with the conduction band. Thus, the gapless edge state is contributed by only one spin channel as a single 1D chiral mode, leading to a quantized anomalous Hall conductance in the bulk gap [15]. The band structure and edge state showing the QAHE (*ABBA* and *ABAB*) and T-broken QSHE (*BAB*) for the other configurations are listed in Supplemental Material, Sec. IV [36].

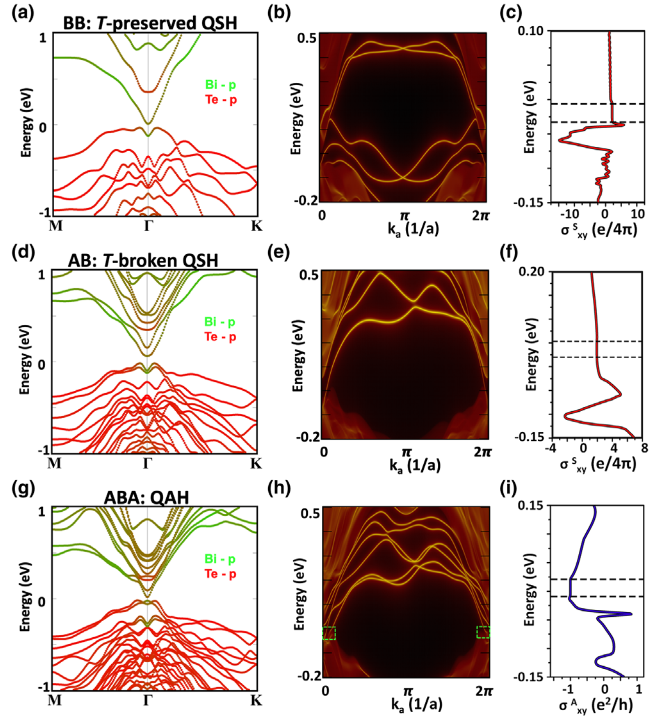

FIG. 3. (a)–(c) Band structure with projection onto different atomic orbitals (a), edge states (b), and quantized spin Hall conductance (c) of *BB* (bilayer Bi_2Te_3) configuration. (d)–(f) Same as (a)–(c) but for the *AB* configuration. (g),(h) Same as (a), (b) but for the *ABA* configuration. (i) Quantized anomalous Hall conductance of the *ABA* configuration.

QAHE design principles.—Our DFT results suggest that the topological properties of the 2D systems fit the phase diagram quite well, which not only indicates that the main physics of the topological phase transitions is successfully captured by our simple model but also provides us rational design principles for the QAHE, as illustrated by Fig. 1(a). We place the configurations as discrete points in the phase diagram as follows. First, beginning with a specific configuration (e.g., *AB*), replacing a B layer with an A layer (e.g., *AA*) leads to upward vertical movement in the phase diagram. Therefore, the *BB*-*AB*-*AA* evolution [red vertical line in Fig. 1(a)] involves gradually adding an exchange field to a 2D T-preserved TI. The exchange field initially makes the band inversions of two spin channels nonequivalent, corresponding to the T-broken QSHE. Then, releasing the band inversion of one spin channel transforms the system into the QAHE phase. Second, adding a nonmagnetic B layer leads to rightward horizontal movement in the phase diagram. As shown by the red horizontal line in Fig. 1(a), the A-*AB*-*BAB* evolution illustrates the phase transition between the NI and T-broken QSHE phases by changing the film thickness.

Some conditions of our continuous model do not exist in certain 2D systems that we choose, such as a uniform exchange field and inversion symmetry. For example, *ABAB* and *ABBA* correspond to the same QAHE point in the phase diagram in terms of the thickness and total magnetization, but while *ABBA* has inversion symmetry, the SIA effect exists in *ABAB*. Previous model Hamiltonian calculations revealed that the presence of SIA tends to release the band inversion in a Chern insulator [26,35], consistent with our DFT-calculated results that both *ABAB* and *ABBA* are Chern insulators with $C = 1$ but that *ABAB* has a smaller bandgap (see Table I). Another effect induced by Rashba SOC is that the 2D model Hamiltonian, Eq. (2), is no longer block diagonal, leading to hybridization between spin-up and spin-down channels. Thus, our DFT-calculated spin Hall conductance for the *AB* configuration is $1.94 \times e/4\pi$, slightly less than the exact quantization. However, by choosing a proper "pseudospin" vector, one can still obtain block-diagonal Eq. (2) with the SIA term and then define a rigorous spin Chern number that is an integer for the T-broken QSH insulator [53].

The growth of new layered magnetic TIs, such as $MnBi_4Te_7$ and $MnBi_6Te_{10}$, enables the realization of different topological states by stacking different building blocks. The question is then how can we propose a candidate configuration or unveil a "magic sequence" of a heterostructure for a critically needed material functionality such as the QAHE? The phase diagram [Fig. 1(a)] helps summarize the design principles. The QAHE region indicates that in most cases, a sufficiently large magnetization is required. Therefore, an FM configuration should be stable or metastable with a slightly higher total energy than the ground state. Due to the existence of a Bi_2Te_3 buffer layer, a much smaller magnetic field than that for $MnBi_2Te_4$ thin films is required to trigger the QAHE in $MnBi_4Te_7$ or $MnBi_6Te_{10}$ films. Such magnetic manipulation can also be achieved by an external magnetic field. By directly applying a magnetic field to the *AB* configuration along the z axis, the phase transition between the T-broken QSHE and QAHE phases also occurs above a critical field $gM = 85$ meV (see Supplemental Material, Sec. V [36]). Additionally, with a fixed magnetization, the QAHE can be realized by increasing the film thickness because the band gap decreases with increasing film thickness, as does the critical exchange field for topological phase transition. Such horizontal regulation can be continuously achieved, thus reaching the QAHE region between *A* and *AB* by an electric field that applies a different on-site energy to real-space separated orbitals. Consequently, through exfoliation of $MnBi_4Te_7$ and $MnBi_6Te_{10}$ with superlatticelike stacking patterns, we can, in principle, discretely reach a large area of the phase diagram to realize the sought functionality, which calls for further experimental confirmation.

We thank Prof. Haizhou Lu, Ni Ni, and Dr. Tong Zhou for helpful discussions. This work was supported by the National Natural Science Foundation of China under Grant No. 11874195, Guangdong Innovative and Entrepreneurial Research Team Program under Grant No. 2017ZT07C062 and Guangdong Provincial Key Laboratory for Computational Science and Material Design under Grant No. 2019B030301001.

H. S., B. X., and Z. C. contributed equally to this work.

*liuqh@sustech.edu.cn

[1] Y. Tokura, K. Yasuda, and A. Tsukazaki, Nat. Rev. Phys. **1**, 126 (2019).
[2] L. Šmejkal, Y. Mokrousov, B. Yan, and A. H. MacDonald, Nat. Phys. **14**, 242 (2018).
[3] F. Tang *et al.*, Nature (London) **569**, 537 (2019).
[4] N. Nagaosa, J. Sinova, S. Onoda, A. H. MacDonald, and N. P. Ong, Rev. Mod. Phys. **82**, 1539 (2010).
[5] C.-X. Liu, S.-C. Zhang, and X.-L. Qi, Annu. Rev. Condens. Matter Phys. **7**, 301 (2016).
[6] C.-Z. Chang *et al.*, Science **340**, 167 (2013).
[7] Z. Qiao, S. A. Yang, W. Feng, W.-K. Tse, J. Ding, Y. Yao, J. Wang, and Q. Niu, Phys. Rev. B **82**, 161414(R) (2010).
[8] H. Zhang, C. Lazo, S. Blügel, S. Heinze, and Y. Mokrousov, Phys. Rev. Lett. **108**, 056802 (2012).
[9] S.-C. Wu, G. Shan, and B. Yan, Phys. Rev. Lett. **113**, 256401 (2014).
[10] K. Dolui, S. Ray, and T. Das, Phys. Rev. B **92**, 205133 (2015).
[11] L. Dong, Y. Kim, D. Er, A. M. Rappe, and V. B. Shenoy, Phys. Rev. Lett. **116**, 096601 (2016).
[12] L. Muechler, E. Liu, Q. Xu, C. Felser, and Y. Sun, arXiv: 1712.08115.
[13] Z. F. Wang, Z. Liu, J. Yang, and F. Liu, Phys. Rev. Lett. **120**, 156406 (2018).
[14] Z. Liu, G. Zhao, B. Liu, Z. F. Wang, J. Yang, and F. Liu, Phys. Rev. Lett. **121**, 246401 (2018).
[15] M. M. Otrokov *et al.*, 2D Mater. **4**, 025082 (2017).
[16] B. Huang *et al.*, Nature (London) **546**, 270 (2017).
[17] C. Gong *et al.*, Nature (London) **546**, 265 (2017).
[18] D. Zhang, M. Shi, T. Zhu, D. Xing, H. Zhang, and J. Wang, Phys. Rev. Lett. **122**, 206401 (2019).
[19] M. M. Otrokov *et al.*, arXiv:1809.07389.
[20] Y. Gong *et al.*, Chin. Phys. Lett. **36**, 076801 (2019).
[21] J. Li, Y. Li, S. Du, Z. Wang, B.-L. Gu, S.-C. Zhang, K. He, W. Duan, and Y. Xu, Sci. Adv. **5**, eaaw5685 (2019).
[22] Y. Deng, Y. Yu, M. Z. Shi, J. Wang, X. H. Chen, and Y. Zhang, arXiv:1904.11468.
[23] C. Liu *et al.*, arXiv:1905.00715.
[24] M. M. Otrokov, I. P. Rusinov, M. Blanco-Rey, M. Hoffmann, A. Yu. Vyazovskaya, S. V. Eremeev, A. Ernst, P. M. Echenique, A. Arnau, and E. V. Chulkov, Phys. Rev. Lett. **122**, 107202 (2019).
[25] K. v. Klitzing, G. Dorda, and M. Pepper, Phys. Rev. Lett. **45**, 494 (1980).
[26] R. Yu, W. Zhang, H.-J. Zhang, S.-C. Zhang, X. Dai, and Z. Fang, Science **329**, 61 (2010).
[27] C. L. Kane and E. J. Mele, Phys. Rev. Lett. **95**, 146802 (2005).
[28] B. A. Bernevig, T. L. Hughes, and S.-C. Zhang, Science **314**, 1757 (2006).

[29] Y. Yang, Z. Xu, L. Sheng, B. Wang, D. Y. Xing, and D. N. Sheng, Phys. Rev. Lett. **107**, 066602 (2011).
[30] C. Hu *et al.*, arXiv:1905.02154.
[31] J. Wu *et al.*, arXiv:1905.02385.
[32] H. Zhang, C.-X. Liu, X.-L. Qi, X. Dai, Z. Fang, and S.-C. Zhang, Nat. Phys. **5**, 438 (2009).
[33] H.-Z. Lu, W.-Y. Shan, W. Yao, Q. Niu, and S.-Q. Shen, Phys. Rev. B **81**, 115407 (2010).
[34] The model parameters of Eq. (1) are listed in the following: $A_0 = 0.287$ eV Å; $B_0 = 0.026$ eV Å; $C_0 = -0.018$ eV; $C_1 = 0.655$ eV Å^2; $C_2 = 4.968$ eV Å^2; $M_0 = -0.153$ eV; $M_1 = 4.000$ eV Å^2; $M_2 = 3.738$ eV Å^2.
[35] H.-Z. Lu, A. Zhao, and S.-Q. Shen, Phys. Rev. Lett. **111**, 146802 (2013).
[36] See Supplemental Material at http://link.aps.org/supplemental/10.1103/PhysRevLett.123.096401 for the parameters of the 2D effective Hamiltonian, first-principles calculation methods, exfoliation energy, band structure and edge states of other 2D configurations, and the topological phase transition of the *AB* configuration by magnetic field, which includes Refs. [37–48].
[37] P. Hohenberg and W. Kohn, Phys. Rev. **136**, B864 (1964).
[38] W. Kohn and L. J. Sham, Phys. Rev. **140**, A1133 (1965).
[39] H. J. Monkhorst and J. D. Pack, Phys. Rev. B **13**, 5188 (1976).
[40] A. I. Liechtenstein, V. I. Anisimov, and J. Zaanen, Phys. Rev. B **52**, R5467 (1995).
[41] G. Kresse and J. Furthmüller, Phys. Rev. B **54**, 11169 (1996).
[42] J. P. Perdew, K. Burke, and M. Ernzerhof, Phys. Rev. Lett. **77**, 3865 (1996).
[43] J. P. Perdew, K. Burke, and M. Ernzerhof, Phys. Rev. Lett. **78**, 1396 (1997).
[44] G. Kresse and D. Joubert, Phys. Rev. B **59**, 1758 (1999).
[45] A. A. Mostofi, J. R. Yates, Y.-S. Lee, I. Souza, D. Vanderbilt, and N. Marzari, Comput. Phys. Commun. **178**, 685 (2008).
[46] N. Marzari, A. A. Mostofi, J. R. Yates, I. Souza, and D. Vanderbilt, Rev. Mod. Phys. **84**, 1419 (2012).
[47] J. H. Jung, C.-H. Park, and J. Ihm, Nano Lett. **18**, 2759 (2018).
[48] Q. Wu, S. Zhang, H.-F. Song, M. Troyer, and A. A. Soluyanov, Comput. Phys. Commun. **224**, 405 (2018).
[49] C.-X. Liu, H. Zhang, B. Yan, X.-L. Qi, T. Frauenheim, X. Dai, Z. Fang, and S.-C. Zhang, Phys. Rev. B **81**, 041307(R) (2010).
[50] W.-Y. Shan, H.-Z. Lu, and S.-Q. Shen, New J. Phys. **12**, 043048 (2010).
[51] Note that dictated by certain relationship between the initial parameters, the slab of a 3D nonmagnetic as a 2D system could be always trivial independent of L, with the band gap approaching zero asymptotically see Ref. [52].
[52] Z. Wang *et al.*, Nano Lett. **19**, 4627 (2019).
[53] H. Li, L. Sheng, and D. Y. Xing, Phys. Rev. Lett. **108**, 196806 (2012).